MNRAS **000**, 000–000 (0000) Preprint 10 December 2015 Compiled using MNRAS LATEX style file v3.0

The *XMM* Cluster Survey: evolution of the velocity dispersion – temperature relation over half a Hubble time

Susan Wilson,[1⋆] Matt Hilton,[1†] Philip J. Rooney,[2] Caroline Caldwell,[3] Scott T. Kay,[4] Chris A. Collins,[3] Ian G. McCarthy,[3] A. Kathy Romer,[2] Alberto Bermeo-Hernandez,[2] Rebecca Bernstein,[5] Luiz da Costa,[6,7] Daniel Gifford,[8] Devon Hollowood,[9] Ben Hoyle,[10] Tesla Jeltema,[9] Andrew R. Liddle,[11] Marcio A. G Maia,[6,7] Robert G. Mann,[11] Julian A. Mayers,[3] Nicola Mehrtens,[12,13] Christopher J. Miller,[8] Robert C. Nichol,[14] Ricardo Ogando,[6,7] Martin Sahlén,[15] Benjamin Stahl,[9] John P. Stott,[16] Peter A. Thomas,[2] Pedro T. P. Viana,[17,18] and Harry Wilcox[14]

[1] *Astrophysics & Cosmology Research Unit, School of Mathematics, Statistics & Computer Science, University of KwaZulu-Natal, Durban 4041, SA*
[2] *Astronomy Centre, University of Sussex, Falmer, Brighton, BN1 9QH, UK*
[3] *Astrophysics Research Institute, Liverpool John Moores University, IC2, Liverpool Science Park, 146 Brownlow Hill, Liverpool, L3 5RF, UK*
[4] *Jodrell Bank Centre for Astrophysics, School of Physics and Astronomy, The University of Manchester, Manchester, M13 9PL, UK*
[5] *Observatories of the Carnegie Institution for Science, 813 Santa Barbara Street, Pasadena, CA 91101, USA*
[6] *Observatório Nacional, Rua Gal. José Cristino 77, Rio de Janeiro, RJ - 22460-040, Brazil*
[7] *Laboratório Interinstitucional de e-Astronomia - LIneA, Rua Gal. José Cristino 77, Rio de Janeiro, RJ - 20921-400, Brazil*
[8] *Astronomy Department, University of Michigan, Ann Arbor, MI 48109, USA*
[9] *Department of Physics and Santa Cruz Institute for Particle Physics, University of California, Santa Cruz, CA 95064, USA*
[10] *Universitaets-Sternwarte, Fakultaet fuer Physik, Ludwig-Maximilians Universitaet Muenchen, Scheinerstr. 1, D-81679 Muenchen, Germany*
[11] *Institute for Astronomy, University of Edinburgh, Royal Observatory, Blackford Hill, Edinburgh, EH9 3HJ, UK*
[12] *George P. and Cynthia Woods Mitchell Institute for Fundamental Physics and Astronomy, Texas A & M University, College Station, TX, 77843-4242 USA*
[13] *Department of Physics and Astronomy, Texas A & M University, College Station, TX, 77843-4242 USA*
[14] *Institute of Cosmology and Gravitation, University of Portsmouth, Dennis Sciama Building, Portsmouth, PO1 3FX, UK*
[15] *BIPAC, Department of Physics, University of Oxford, Denys Wilkinson Building, 1 Keble Road, Oxford OX1 3RH, UK*
[16] *Sub-department of Astrophysics, Department of Physics, University of Oxford, Denys Wilkinson Building, Keble Road, Oxford OX1 3RH, UK*
[17] *Instituto de Astrofísica e Ciências do Espaço, Universidade do Porto, CAUP, Rua das Estrelas, 4150-762 Porto, Portugal*
[18] *Departamento de Física e Astronomia, Faculdade de Ciências, Universidade do Porto, Rua do Campo Alegre, 687, 4169-007 Porto, Portugal*

Draft version: 10 December 2015

ABSTRACT

We measure the evolution of the velocity dispersion–temperature (σ_v–T_X) relation up to $z = 1$ using a sample of 38 galaxy clusters drawn from the *XMM* Cluster Survey. This work improves upon previous studies by the use of a homogeneous cluster sample and in terms of the number of high redshift clusters included. We present here new redshift and velocity dispersion measurements for 12 $z > 0.5$ clusters observed with the GMOS instruments on the Gemini telescopes. Using an orthogonal regression method, we find that the slope of the relation is steeper than that expected if clusters were self-similar, and that the evolution of the normalisation is slightly negative, but not significantly different from zero ($\sigma_v \propto T^{0.86\pm0.14}E(z)^{-0.37\pm0.33}$). We verify our results by applying our methods to cosmological hydrodynamical simulations. The lack of evolution seen from the data suggests that the feedback does not significantly heat the gas, a result that is consistent with simulations including radiative cooling.

Key words: galaxies: clusters: general, galaxies: clusters: intracluster medium, galaxies: distances and redshifts, X-rays: galaxies: clusters, cosmology: miscellaneous

1 INTRODUCTION

Clusters of galaxies are the largest coherent gravitationally bound objects in our Universe. By studying galaxy clusters, information

⋆ E-mail: swilson072@gmail.com
† E-mail: hiltonm@ukzn.ac.za

can be gained about the formation of galaxies, and the effect of ongoing processes such as merging and AGN feedback. They can also be used as a probe of cosmology by studying the evolution of their number density with mass and redshift (e.g., Vikhlinin et al. 2009; Hasselfield et al. 2013; Reichardt et al. 2013; Planck Collaboration et al. 2015). However, the mass of galaxy clusters is not a quantity that can be directly measured, and therefore it needs to be determined using observable mass tracers such as X-ray properties (e.g., luminosity and temperature), the Sunyaev-Zel'dovich (SZ) effect signal, and optical properties, such as richness, line-of-sight velocity dispersion of member galaxies, and shear due to gravitational lensing (e.g., Ortiz-Gil et al. 2004; Vikhlinin et al. 2006; Rozo et al. 2009; Sifón et al. 2013; Nastasi et al. 2014; von der Linden et al. 2014; Hoekstra et al. 2015).

In this paper we focus on the relationship between the velocity dispersion of member galaxies (σ_v) and the X-ray temperature (T_X) of the intracluster medium (ICM). Since the velocity dispersion is a measure of the kinetic energy of the galaxies in the cluster, and temperature is related to the kinetic energy of the gas, both the gas and galaxies are tracers of the gravitational potential. One would expect a self-similar relationship of the form $\sigma_v \propto T^{0.5}$, if clusters were formed purely due to the action of gravity (Quintana & Melnick 1982; Kaiser 1986; Voit 2005). However, almost all previous studies of the relation have found a steeper power-law slope than this (see Table 1). The relation is also not expected to evolve with redshift. To date this has been tested only by Wu et al. (1998) and Nastasi et al. (2014). Even then, all but four clusters in the Wu et al. (1998) sample are at $z < 0.5$. Nastasi et al. (2014) made a measurement of the relation at $0.6 < z < 1.5$ using a sample of 12 clusters, obtaining results consistent with previous studies at low redshift.

One may expect evolution in cluster scaling relations due to the increase of star formation and AGN activity at high redshift (e.g., Silverman et al. 2005; Magnelli et al. 2009), or due to the increase in frequency of galaxy cluster mergers with increasing redshift (e.g., Cohn & White 2005; Kay et al. 2007; Mann & Ebeling 2012). Galaxy cluster mergers are among the most energetic events in the Universe, and simulations have shown that these could result in the boosting of cluster X-ray temperatures (e.g., Ritchie & Thomas 2002; Randall et al. 2002; Poole et al. 2007). All of these processes add energy into the ICM, and so we might expect to see an overall increase in the average temperatures of galaxy clusters above that expected from the self-similar case at a given redshift.

There have been many studies of the luminosity – temperature relation ($L_X - T$), though there is no concensus on how it evolves with redshift. Some studies have found that the evolution of the normalisation of this relation is consistent with self-similarity (e.g., Vikhlinin et al. 2002; Lumb et al. 2004; Maughan et al. 2006), while other studies have found zero or negative evolution (e.g., Ettori et al. 2004; Branchesi et al. 2007; Hilton et al. 2012; Clerc et al. 2012, 2014). Maughan et al. (2012) also found that the evolution of the $L_X - T$ relation was not self-similar, but concluded that this could plausibly be explained by selection effects.

In this paper, we study a sample of 38 $z < 1.0$ galaxy clusters drawn from the *XMM* Cluster Survey (XCS; Mehrtens et al. 2012). We divide the sample into two groups: a low redshift sample ($0.0 < z < 0.5$), and a high redshift sample ($0.5 < z < 1.0$), with an equal number of clusters in each, and then proceed to test for evolution in the $\sigma_v - T$ relation. We describe the sample and processing of the optical and X-ray data in Section 2. Section 3 discusses the method used to determine cluster membership and for measuring the velocity dispersion and describes the methods used for fitting the σ_v–T relation, and we present our results in Section 4. We discuss our findings in Section 5 and present our conclusions in Section 6.

We assume a cosmology with $\Omega_m = 0.27$, $\Omega_\Lambda = 0.73$, and $H_0 = 70\,\mathrm{km\,s^{-1}\,Mpc^{-1}}$ throughout.

2 SAMPLE AND DATA REDUCTION

The cluster sample for this work is drawn from XCS, a serendipitous X-ray cluster survey being conducted using archival *XMM-Newton* data. Data Release 1 (DR1) of the XCS is described in Mehrtens et al. (2012). The overall aims of the XCS project are to measure cosmological parameters through the evolution of the cluster mass function with redshift (Sahlén et al. 2009), study the evolution of galaxies in clusters (Collins et al. 2009; Hilton et al. 2009, 2010; Stott et al. 2010) and investigate the X-ray scaling relations as a way to study the evolution of the cluster gas with redshift (Hilton et al. 2012).

The XCS Automated Pipeline Algorithm (XAPA) described in Lloyd-Davies et al. (2011) was used to search the XMM archive for cluster candidates. Mehrtens et al. (2012) describes confirmation of a subset of these candidates as clusters using the combination of data from the literature and optical follow-up observations. This left a final sample of 503 X-ray confirmed galaxy clusters, 255 which were previously unknown and 356 of which were new X-ray detections. Of these, 464 have redshift estimates, and 402 have temperature measurements.

For XCS-DR1 the cluster-averaged X-ray temperatures (T_X) were measured using an automated pipeline described in detail in Lloyd-Davies et al. (2011). In summary this pipeline operates as follows: spectra were generated in the 0.3-7.9 keV band using photons in the XAPA source ellipse; an in-field background subtraction method was used; and model fitting was done inside XSPEC (Schafer 1991) using an absorbed MEKAL (Mewe & Schrijver 1986) model and Cash statistics (Cash 1979). In the fit, the hydrogen column density was fixed to the Dickey (1990) value and the metal abundance to 0.3 times the Solar value. For this paper we have updated the T_X values compared to Mehrtens et al. (2012). The pipeline is very similar to that described in Lloyd-Davies et al. (2011), but using updated versions of the XMM calibration and XSPEC.

For this paper both the samples were constructed from XCS DR1, except for one of the high redshift sample clusters (XMMXCS J113602.9-032943.2) which is a previously unreported XCS cluster detection. Fig. 1 shows the redshift and temperature distributions of the two samples.

2.1 Low redshift sample

The low redshift sample contains 19 clusters whose properties can be found in Table 3. In order to obtain this sample we excluded all clusters from the DR1 sample that did not have temperatures or which had a redshift $z > 0.5$, leaving us with a sample of 320 clusters. We performed a search in NED[1] for galaxies surrounding each cluster with known spectroscopic redshifts. We excluded galaxies located at projected radial distance $> R_{200}$ (the radius within which

[1] This research has made use of the NASA/IPAC Extragalactic Database (NED) which is operated by the Jet Propulsion Laboratory, California Institute of Technology, under contract with the National Aeronautics and Space Administration.

Table 1. Previous measurements of the velocity dispersion–temperature relation. Here the relation is in the form $\sigma_v = 10^A T^B$, where σ_v is measured in km s^{-1} and T is measured in keV.

Paper	Number of clusters	A	B	Redshift range	Fitting method
Edge & Stewart (1991)	23	2.60 ± 0.08	0.46 ± 0.12	$z < 0.1$	Least squares
Lubin & Bahcall (1993)	41	2.52 ± 0.07	0.60 ± 0.11	$z < 0.2$	χ^2
Bird et al. (1995)	22	2.50 ± 0.09	0.61 ± 0.13	$z < 0.1$	Bisector
Girardi et al. (1996)	37	2.53 ± 0.04	0.61 ± 0.05	$z < 0.2$	Bisector
Ponman et al. (1996)	27	2.54 ± 0.04	0.55 ± 0.05	$z < 0.15$	Bisector
White et al. (1997)	35	2.53 ± 0.08	0.60 ± 0.10	$z < 0.2$	Orthogonal
Wu et al. (1998)	94	2.47 ± 0.06	0.67 ± 0.09	$z < 0.9$	Orthogonal
Wu et al. (1998)	110	2.57 ± 0.03	0.49 ± 0.05	$z < 0.1$	Orthogonal
Wu et al. (1998)	39	2.57 ± 0.08	0.56 ± 0.09	$0.1 < z < 0.9$	Orthogonal
Wu et al. (1999)	92	2.49 ± 0.03	0.64 ± 0.02	$z < 0.45$	Orthogonal
Xue & Wu (2000)	109	2.53 ± 0.03	0.58 ± 0.05	$z < 0.2$	Orthogonal
Nastasi et al. (2014)	12	2.47 ± 0.19	0.64 ± 0.34	$0.64 < z < 1.46$	Bisector

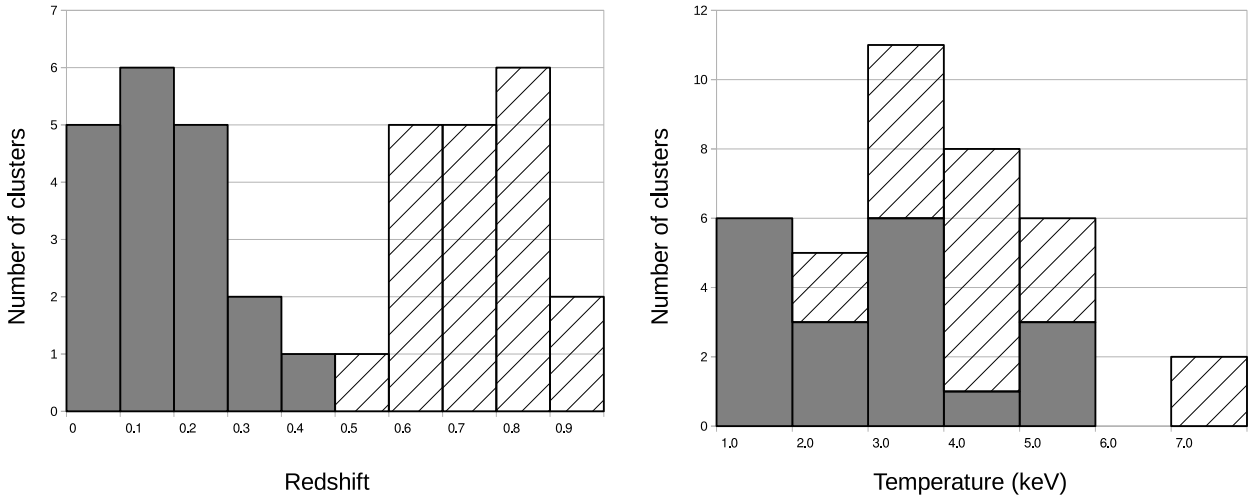

Figure 1. The redshift and temperature distributions of the low and high redshift cluster samples used in this work. The solid grey marks the low redshift sample ($z < 0.5$) and the shading with diagonal lines marks the high redshift sample ($z > 0.5$). Note that the high redshift sample contains more high temperature clusters than the low redshift sample.

the mean density is 200 times the critical density of the Universe at the cluster redshift) as such galaxies are unlikely to be cluster members. To ensure we did not exclude possible members, for this initial step R_{200} was calculated using a fiducial velocity dispersion of 2000 km s^{-1} following Finn et al. (2005),

$$R_{200}\,(\mathrm{Mpc}) = 2.47 \frac{\sigma_v}{1000\,\mathrm{km\,s^{-1}}} \frac{1}{\sqrt{\Omega_\Lambda + \Omega_0 (1+z)^3}}. \quad (1)$$

Here σ_v is the line of sight velocity dispersion (see Section 3.1.3) and z is the redshift of the cluster. Equation 1 assumes that the galaxy velocity distribution follows an isothermal sphere dark matter profile. The fiducial R_{200} values span the range 2–4 Mpc. Section 3.1.2 below describes how this initial cluster membership selection was refined to give the final cluster members from which the velocity dispersion was measured.

2.2 High redshift sample

The high redshift sample is made up of 19 clusters whose properties can be found in Table 3. Member redshifts were determined from observations using the Gemini telescopes for 12 of these clusters (see Section 2.2.1). The other seven clusters used data obtained from Nastasi et al. (2014). They drew both on new observations and on existing data. For example, the observations of three of the Nastasi et al. (2014) clusters we have used in this paper (XMMXCS J105659.5-033728.0, XMMXCS J113602.9-032943.2 and XMMXCS J182132.9+682755.0 in Table 3) were presented in Tran et al. (1999) respectively. The observations of the other 4 clusters we have used in this paper were presented for the first time in Nastasi et al. (2014). These four were discovered independently (to XCS) by the XMM Newton Distant Cluster Project (XDCP; Fassbender et al. 2011). Nastasi et al. (2014) also presented galaxy redshift data for another six XDCP clusters, however we have not used those in this paper because there are insufficient galaxies to derive an accurate velocity dispersion[2]. For the seven clusters that relied on Nastasi et al. (2014) data, new temperatures were obtained using XCS pipelines and the velocity dispersion was recalculated using the Nastasi et al. (2014) cluster redshift together with the method described in Section 3.

[2] The methodology described in Section 3 was applied to these six clusters before they were excluded from our study.

2.2.1 *Observations*

Observations of 12 $z > 0.5$ clusters were obtained using the Gemini Multi Object Spectographs (GMOS) on both the Gemini telescopes from 2010 to 2012. The nod-and-shuffle mode (Glazebrook & Bland-Hawthorn 2001) was used to allow better sky subtraction and shorter slit lengths when compared to conventional techniques. For all observations the R400 grating and OG515 order blocking filter were used, giving wavelength coverage of 5400 – 9700 Å. A total of 30 masks were observed with a varying number of target slitlets. Each slitlet had length $3''$ and width $1''$. Target galaxies were selected to be fainter than the brightest cluster galaxy, on the basis of *i*-band pre-imaging obtained from Gemini. Observations at three different central wavelengths (7500, 7550 and 7600 Å) were used to obtain coverage over the gaps between the GMOS CCDs. For all observations an 85 percentile image quality and 50 percentile sky transparency were requested. The details of the individual observations are given in Table A1.

2.2.2 *Spectroscopic data reduction*

The data were reduced in a similar manner to Hilton et al. (2010), using PYRAF and the Gemini IRAF[2] package. We used the tools from this package to subtract bias frames; make flat fields; apply flat field corrections and create mosaic images. We then applied nod-and-shuffle sky subtraction using the `gnsskysub` task. Wavelength calibration was determined from arc frames taken between the science frames, using standard IRAF tasks. All data were then combined using a median, rejecting bad pixels using a mask constructed from the nod-and-shuffle dark frames. Finally, we combined the pairs of spectra corresponding to each nod position, and extracted one-dimensional spectra using a simple boxcar algorithm.

2.2.3 *Galaxy redshift measurements*

We measured galaxy redshifts from the spectra by cross-correlation with SDSS spectral templates[3] using the RVSAO/XCSAO package for IRAF (Kurtz & Mink 1998). XCSAO implements the method described by Tonry & Davis (1979). The spectra were compared to six different templates over varying redshifts with the final redshift measurement being determined after visual inspection. Redshifts were assigned a quality flag according to the following scheme: $Q = 3$ corresponds to two or more strongly detected features; $Q = 2$ refers to one strongly detected or two weakly detected features; $Q =$ 1 one weakly detected feature and $Q = 0$ when no features could be identified. Only galaxies with a quality rating of $Q \geqslant 2$ were used in this study because these have reasonably secure redshifts. Fig.2 shows spectra of some member galaxies of the cluster XMMXCS J025006.4-310400.8 as an example. Tables of redshifts for galaxies in each cluster field can be found in Appendix B.

[2] IRAF is distributed by the National Optical Astronomy Observatories,which are operated by the Association of Universities for Research in Astronomy, Inc., under cooperative agreement with the National Science Foundation.

[3] http://www.sdss.org/dr7/algorithms/spectemplates/index. html

3 ANALYSIS

3.1 Membership determination and velocity dispersion measurements

In this section we describe the methodology used to determine cluster membership and calculate the velocity dispersion of each cluster.

3.1.1 *Cluster redshifts*

For all of the clusters an estimate of the redshift is known either from the literature or from previous observations and this is used as a starting point. The peculiar velocity of each of the galaxies is calculated relative to this redshift estimate using

$$v_i = c \times \frac{z_i - \bar{z}}{1 + \bar{z}}, \tag{2}$$

where v_i is the peculiar velocity of the ith galaxy, z_i is the redshift of the ith galaxy, $\bar{z}$ is the redshift of the cluster and c is the speed of light. Extreme foreground and background sources were removed by applying a $3000\,\mathrm{km\,s^{-1}}$ cut with respect to the cluster redshift and then the redshift was recalculated using the biweight location method described by Beers et al. (1990). This process was iterated until the redshift converged.

3.1.2 *Cluster membership*

A fixed gapper method, similar to that of Fadda et al. (1996) and Crawford et al. (2014), was applied to determine which galaxies are cluster members. The reasoning behind this method is that by studying a histogram of the redshifts of possible members there should be a clear distinction between the cluster and the fore/background galaxies. Therefore we can exclude interlopers by finding the velocity difference between adjacent galaxies and setting a fixed gap that should not be exceeded. De Propris et al. (2002) found this optimum gap to be $1000\,\mathrm{km\,s^{-1}}$, which avoids the merging of subclusters but also prevents the breaking up of real systems into smaller groups. Therefore all our galaxies were sorted by peculiar velocity and the difference between all adjacent pairs was calculated. Any galaxies which had a difference between adjacent galaxies of greater than $1000\,\mathrm{km\,s^{-1}}$ were considered interlopers and were removed. This process was iterated until the number of galaxies converged.

3.1.3 *Velocity dispersion*

We used our confirmed galaxy cluster members to calculate an initial estimate of the velocity dispersion of each cluster using the biweight scale method described in Beers et al. (1990). We then calculated R_{200} using Equation 1, and excluded all galaxies located at projected cluster-centric radial distances outside R_{200}. The velocity dispersion of each cluster was then recalculated. This final radial cut did not remove more than two galaxies from the final sample for each cluster. Tables 2 and 3 list the final redshifts, velocity dispersions, and R_{200} values for the low and high redshift samples respectively.

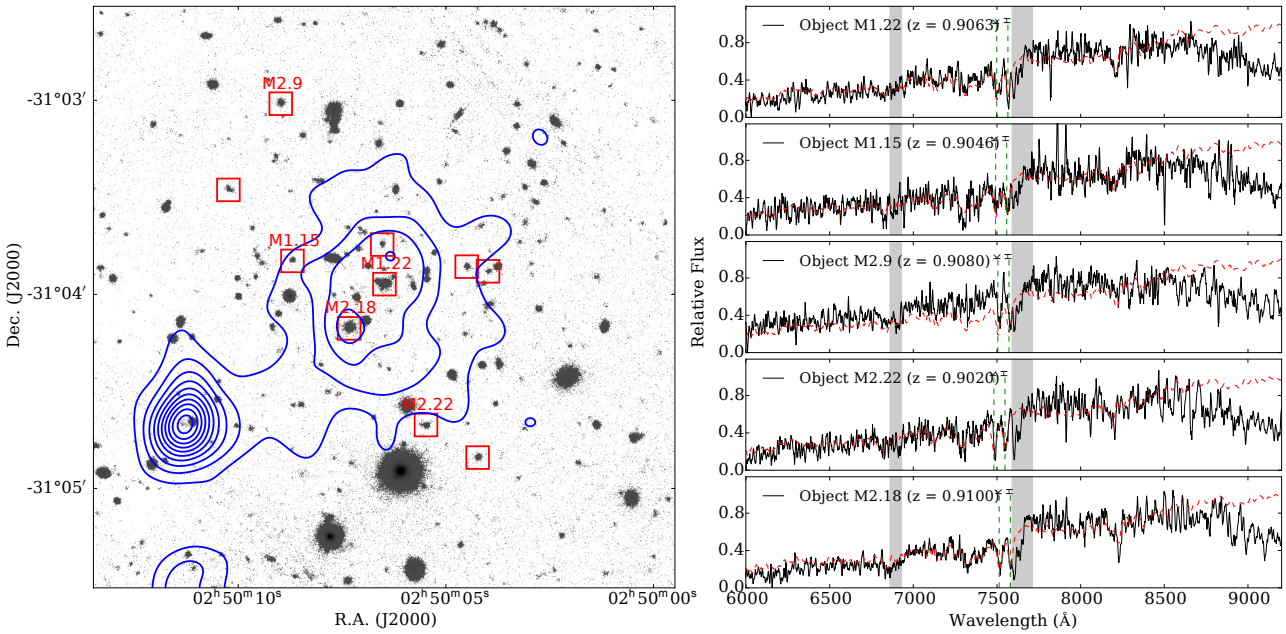

Figure 2. The z=0.91 cluster XMMXCS J025006.4 – 310400.8. The left hand panel shows the SDSS optical image overlayed with the X–ray contours in blue. The red squares represent possible galaxy cluster members. Each possible member is labeled Mx.y, where x is the mask number and y is the object ID.The right hand panel shows the spectra of a subset of these galaxies. The black line corresponds to the spectra obtained from Gemini and the red dashed line is the best fit SDSS template. The green dotted vertical lines show the identified spectral lines.

Table 2. Low redshift sample ($0.0 < z < 0.5$): column 1 gives the name of the XCS Cluster, columns 2 and 3 give its J2000 right ascension and declination. Column 4 gives the redshift and columns 5 gives the temperature with its positive and negative 1σ uncertainty. Column 6 gives the number of confirmed members and columns 7 and 8 give the calculated velocity dispersion and R_{200} respectively.

Name	RA (J2000)	Dec (J2000)	z	T (keV)	Members	σ_v (km s^{-1})	R_{200} (Mpc)
XMMXCS J000013.9-251052.1	$00^h00^m13.9^s$	-25°10′52.1″	0.0845	$1.80^{+0.40}_{-0.20}$	19	410 ± 80	1.11
XMMXCS J003430.1-431905.6	$00^h34^m30.1^s$	-43°19′05.6″	0.3958	$3.50^{+0.20}_{-0.20}$	22	920 ± 150	1.96
XMMXCS J005603.0-373248.0	$00^h56^m03.0^s$	-37°32′48.0″	0.1659	$5.20^{+0.30}_{-0.20}$	22	900 ± 140	2.06
XMMXCS J015315.0+010214.2	$01^h53^m15.0^s$	+01°02′14.2″	0.0593	$1.08^{+0.02}_{-0.02}$	12	240 ± 80	0.55
XMMXCS J072054.3+710900.5	$07^h20^m54.3^s$	+71°09′00.5″	0.2309	$2.90^{+0.50}_{-0.40}$	29	550 ± 60	1.20
XMMXCS J081918.6+705457.5	$08^h19^m18.6^s$	+70°54′57.5″	0.2298	$3.00^{+0.80}_{-0.60}$	19	410 ± 70	0.83
XMMXCS J094358.2+164120.7	$09^h43^m58.2^s$	+16°41′20.7″	0.2539	$1.50^{+0.40}_{-0.20}$	27	590 ± 90	1.54
XMMXCS J095957.6+251629.0	$09^h59^m57.6^s$	+25°16′29.0″	0.0523	$1.40^{+0.05}_{-0.05}$	15	510 ± 220	1.79
XMMXCS J100047.4+013926.9	$10^h00^m47.4^s$	+01°39′26.9″	0.2202	$3.30^{+0.20}_{-0.20}$	16	560 ± 140	1.41
XMMXCS J100141.7+022539.8	$10^h01^m41.7^s$	+02°25′39.8″	0.1233	$1.43^{+0.06}_{-0.03}$	26	590 ± 130	1.05
XMMXCS J104044.4+395710.4	$10^h40^m44.4^s$	+39°57′10.4″	0.1389	$3.54^{+0.03}_{-0.03}$	17	860 ± 150	2.12
XMMXCS J111515.6+531949.5	$11^h15^m15.6^s$	+53°19′49.5″	0.4663	$5.40^{+1.50}_{-0.90}$	16	910 ± 310	1.75
XMMXCS J115112.0+550655.5	$11^h51^m12.0^s$	+55°06′55.5″	0.0791	$1.66^{+0.04}_{-0.04}$	16	330 ± 100	1.50
XMMXCS J123144.4+413732.0	$12^h31^m44.4^s$	+41°37′32.0″	0.1735	$2.70^{+0.60}_{-0.40}$	10	480 ± 100	1.26
XMMXCS J151618.6+000531.3	$15^h16^m18.6^s$	+00°05′31.3″	0.1200	$5.40^{+0.10}_{-0.10}$	35	870 ± 220	2.01
XMMXCS J161132.7+541628.3	$16^h11^m32.7^s$	+54°16′28.3″	0.3372	$4.60^{+1.20}_{-0.80}$	12	790 ± 150	1.69
XMMXCS J163015.6+243423.2	$16^h30^m15.6^s$	+24°34′23.2″	0.0625	$3.50^{+0.60}_{-0.40}$	62	710 ± 130	2.20
XMMXCS J223939.3-054327.4	$22^h39^m39.3^s$	-05°43′27.4″	0.2451	$2.80^{+0.20}_{-0.20}$	68	560 ± 70	1.32
XMMXCS J233757.0+271121.0	$23^h37^m57.0^s$	+27°11′21.0″	0.1237	$3.40^{+0.60}_{-0.40}$	12	460 ± 110	1.49

3.2 Fitting the velocity dispersion – temperature relation

To determine the scaling relation between the velocity dispersion and temperature, we fitted a power law of the form

$$\log\left(\frac{\sigma_v}{1000\,\mathrm{km\,s^{-1}}}\right) = A + B\log\left(\frac{T}{5\,\mathrm{keV}}\right) + C\log E(z). \qquad (3)$$

Here, 5 keV and 1000 km s^{-1} are the pivot temperature and velocity dispersion respectively for our fit. These were chosen to reduce the covariance between the normalisation A and the slope B, and for ease of comparison to previous studies. In the above, evolution of the normalisation is parametrised as $E(z)^C$, where $E(z) = \sqrt{\Omega_m(1+z)^3+\Omega_\Lambda}$ describes the redshift evolution of the

Table 3. High redshift sample ($0.5 < z < 1.0$): all columns are as explained in Table 2. The superscripts in column one indicate the origin of redshift data when it did not come from our own observations. [1] also known as MS1054-03 was observed with Keck for 8.6 hours (Tran et al. 1999). [2] was observed with Keck (Donahue et al. 1999). [3] also known as RXJ1821.6+6827 was observed with CFHT, Keck and the 2.2 m telescope at the University of Hawaii (Gioia et al. 2004). [4] are all clusters taken from the XDCP survey and were observed with the VLT–FORS2 spectograph (Nastasi et al. 2014).

Name	RA (J2000)	Dec (J2000)	z	T (keV)	Members	σ_v (km s^{-1})	R_{200} (Mpc)
[4] XMMXCS J000216.1-355633.8	$00^h02^m16.1^s$	-35°56′33.8″	0.7709	$4.83^{+1.01}_{-0.76}$	13	1100 ± 191	1.77
XMMXCS J005656.6-274031.9	$00^h56^m56.6^s$	-27°40′31.9″	0.5601	$3.30^{+0.94}_{-0.63}$	15	380 ± 60	0.66
XMMXCS J015241.1-133855.9	$01^h52^m41.1^s$	-13°38′55.9″	0.8268	$3.23^{+0.38}_{-0.31}$	29	840 ± 150	1.33
XMMXCS J021734.7-051326.9	$02^h17^m34.7^s$	-05°13′26.9″	0.6467	$2.23^{+0.90}_{-0.44}$	12	620 ± 210	1.11
XMMXCS J025006.4-310400.8	$02^h50^m06.4^s$	-31°04′00.8″	0.9100	$4.50^{+1.33}_{-0.88}$	13	1120 ± 260	1.66
XMMXCS J030205.1-000003.6	$03^h02^m05.1^s$	-00°00′03.6″	0.6450	$5.82^{+2.09}_{-1.32}$	16	610 ± 180	1.04
XMMXCS J095417.1-173805.9	$09^h54^m17.1^s$	-17°38′05.9″	0.8272	$3.65^{+0.62}_{-0.51}$	10	940 ± 310	1.42
XMMXCS J095940.7+023113.4	$09^h59^m40.7^s$	+02°31′13.4″	0.7291	$5.02^{+0.68}_{-0.55}$	25	470 ± 90	0.88
[1] XMMXCS J105659.5-033728.0	$10^h56^m59.5^s$	-03°37′28.0″	0.8336	$7.57^{+0.43}_{-0.40}$	29	1010 ± 120	1.57
XMMXCS J112349.4+052955.1	$11^h23^m49.4^s$	+05°29′55.1″	0.6550	$4.62^{+1.55}_{-0.95}$	17	600 ± 210	1.05
XMMXCS J113602.9-032943.2	$11^h36^m02.9^s$	-03°29′43.2″	0.8297	$3.32^{+1.20}_{-0.78}$	21	700 ± 110	1.06
[2] XMMXCS J114023.0+660819.0	$11^h40^m23.9^s$	+66°08′19.0″	0.7855	$7.47^{+0.92}_{-0.77}$	22	950 ± 100	1.51
[4] XMMXCS J124312.2-131307.2	$12^h43^m12.2^s$	-13°13′07.2″	0.7910	$4.92^{+2.93}_{-1.54}$	11	790 ± 460	1.19
XMMXCS J134305.1-000056.8	$13^h43^m05.1^s$	-00°00′56.8″	0.6894	$4.49^{+0.72}_{-0.57}$	23	920 ± 170	1.72
XMMXCS J145009.3+090428.8	$14^h50^m09.3^s$	+09°04′28.8″	0.6412	$3.84^{+0.66}_{-0.55}$	22	630 ± 90	1.07
[3] XMMXCS J182132.9+682755.0	$18^h21^m32.9^s$	+68°27′55.0″	0.8166	$4.49^{+0.79}_{-0.56}$	19	860 ± 130	1.34
XMMXCS J215221.0-273022.6	$21^h52^m21.0^s$	-27°30′22.6″	0.8276	$2.18^{+0.67}_{-0.45}$	15	530 ± 150	0.86
XMMXCS J230247.7+084355.9	$23^h02^m47.7^s$	+08°43′55.9″	0.7187	$5.29^{+0.59}_{-0.50}$	22	1010 ± 130	1.60
[4] XMMXCS J235616.4-344144.3	$23^h56^m16.4^s$	-34°41′44.3″	0.9391	$4.57^{+0.48}_{-0.41}$	10	670 ± 260	0.91

Hubble parameter. For the self similar case, $B = 0.5$ and $C = 0$ are expected.

Similarly to Hilton et al. (2012), the best fit values for these parameters were found using Markov Chain Monte-Carlo (MCMC) with the Metropolis algorithm. Both orthogonal and bisector regression methods were used. For the orthogonal method, the probability for a given cluster to be drawn from the model scaling relation is

$$P_{\rm model} = \frac{1}{\sqrt{2\pi(\Delta r^2 + \Delta S^2)}} \exp\left[\frac{-(r - r_{\rm model})^2}{2(\Delta r^2 + \Delta S^2)}\right], \quad (4)$$

where $r - r_{\rm model}$ is the orthogonal distance of the cluster from the model relation, Δr is the error on the orthogonal distance and S is the intrinsic scatter orthogonal to the model relation. Δr is calculated from the projection in the direction orthogonal to the model line of the ellipse defined by the errors on $\log\sigma_v$ and $\log T$.

For the bisector method, the intrinsic scatter and measurement errors are treated independently for each axis. Therefore in the equation for $P_{\rm model}$, $r_{\rm model}$ is replaced by

$$y_{\rm model} = \log\left(\frac{\sigma_v}{1000\,{\rm km\,s^{-1}}}\right) - \left[A + B\log\left(\frac{T}{5\,{\rm keV}}\right) + C\log E(z)\right], \quad (5)$$

and

$$x_{\rm model} = \log\left(\frac{T}{5\,{\rm keV}}\right) - \left[\frac{\log\left(\frac{\sigma_v}{1000\,{\rm km\,s^{-1}}}\right) - A - C\log E(z)}{B}\right], \quad (6)$$

where r and Δr are replaced by x, Δx or y, Δy as appropriate. The intrinsic scatter S is replaced by two parameters S_x and S_y.

For both methods, the likelihood $\mathcal{L}$ of a given model is simply the product of $P_{\rm model}$ for each cluster in the sample, i.e., in the orthogonal case

$$\mathcal{L}(\sigma_v, T | A, B, C, S) \propto P_{\rm prior}(A, B, C, S) \prod_i P_{{\rm model},i}, \quad (7)$$

Table 4. Priors on $\sigma_v - T$ relation fit parameters

Parameter	Uniform Prior	Notes
A	(-5.0,5.0)	-
B	(0.0,2.0)	-
C	(-1.0,1.0)	-
S	(0.01,1.0)	Orthogonal method only
S_x	(0.01,1.0)	Bisector method only
S_y	(0.01,1.0)	Bisector method only

where we assume generous, uniform priors on each parameter, as listed in Table 4.

4 RESULTS

4.1 Evolution of the slope and intrinsic scatter

For the model given in Equation 3, it is assumed that the slope (parameter B) is not evolving with redshift. To test this, the σ_v–T relation was fitted with $C = 0$ in two redshift bins, $0.0 < z < 0.5$ and $0.5 < z < 0.9$, with 19 clusters in each bin. The parameters A, B and S were obtained using the MCMC method described above for the high and low redshift samples individually. The results for this are shown in Fig. 3.

Using the orthogonal method we found $B = 1.12 \pm 0.41$ for the high redshift sample and $B = 0.89 \pm 0.16$ for the low redshift sample. However, we found that the slope of the relation for the high redshift sample is unconstrained if the prior on B is relaxed further. We assume for the remainder of this paper that the slope does not evolve with redshift, though clearly either a larger sample or more accurate measurements of individual clusters are needed to confirm that this is true.

The intrinsic scatter is $S = 0.05 \pm 0.02$ for the low redshift sample and $S = 0.08 \pm 0.04$ for the high redshift sample. Therefore there is no evidence that the intrinsic scatter varies with redshift.

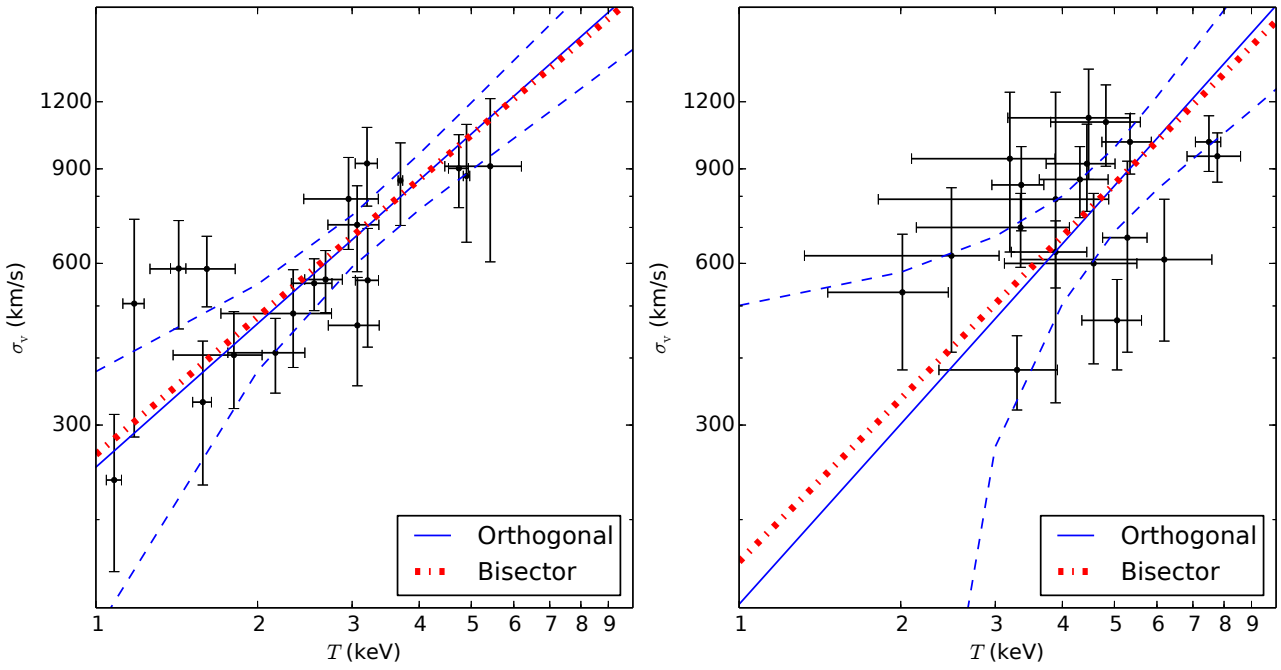

Figure 3. The σ_v–T relation assuming no evolution, i.e., $C = 0$ in Equation 3, for low (left - $0.0 < z < 0.5$) and high (right- $0.5 < z < 0.9$) redshift samples. The solid blue line shows an orthogonal regression fit to the data with the dashed line representing the 95 % confidence interval. The dot-dashed line shows a bisector regression fit to the data (see Section 3.2). A model of the form seen in Equation 3 was used in the Metropolis algorithm to determine a line of best (see Section 4.1).

Table 5. Best-fit σ_v–T scaling relation parameters using both the orthognal and bisector regression methods (see Section 3.2).

Method	Parameter	Low Redshift	High Redshift	Combined (no evolution)	Combined (with evolution)
Orthogonal	A	0.02 ± 0.06	-0.08 ± 0.05	-0.05 ± 0.04	0.02 ± 0.05
	B	0.89 ± 0.16	1.12 ± 0.41	0.72 ± 0.12	0.86 ± 0.14
	S	0.05 ± 0.03	0.08 ± 0.04	0.06 ± 0.03	0.06 ± 0.03
	C	0	0	0	-0.37 ± 0.33
Bisector	A	0.02 ± 0.04	-0.07 ± 0.03	-0.04 ± 0.02	0.02 ± 0.04
	B	0.85 ± 0.11	1.01 ± 0.17	0.77 ± 0.08	0.86 ± 0.09
	S_x	0.15 ± 0.03	0.19 ± 0.03	0.15 ± 0.02	0.14 ± 0.02
	S_y	0.07 ± 0.03	0.12 ± 0.04	0.09 ± 0.02	0.09 ± 0.02
	C	0	0	0	-0.49 ± 0.25

4.2 Evolution of the normalisation

To test for the evolution of the normalisation (parameter A in Equation 3), the low and high redshift samples were combined and C was allowed to vary in the MCMC analysis. The results obtained are shown by the the scaling relation plot in Fig. 4.2. We found $C = -0.53 \pm 0.27$, meaning that for a given σ_v, a higher T is obtained at higher redshift. However, the no evolution relation falls within the 95 per cent confidence interval and therefore we conclude that there is no significant evidence in favour of evolution.

We also applied a statistical test known as the Akaike information criterion (AIC) to determine whether the model with or without evolution (Fig. 4) was preferred. The AIC estimates the quality of each model relative to each other and is therefore a means of model selection. It is defined by (Burnham & Anderson 2002) as

$$\mathrm{AIC} = 2k - 2\ln(\mathcal{L}), \tag{8}$$

where $\mathcal{L}$ is the maximised likelihood function (Equation 7) and k is the number of free parameters. The AIC includes a penalty for using extra parameters as a way to discourage overfitting and rewards goodness of fit based on the likelihood function. Therefore the lower the value of the AIC, the better the fit. For the combined sample with the no evolution model the AIC value was -64.6 and when the fourth parameter for evolution (C) was included this increased to -62.1. Therefore, combining this with the results from the σ_v–T relation fit, it can be concluded that the preferred model is the one with no evolution.

5 DISCUSSION

5.1 Comparison with previous results

Table 5 and Figs.3–4.2 present the results of applying the orthogonal and bisector fitting methods to the low redshift, high redshift, and combined samples. We see that the bisector and orthogonal method give very similar results especially for our total sample without evolution. Hogg et al. (2010) suggests that the bisector method should be avoided, as by simply finding the difference between a forward and reverse fitting method large systematic errors

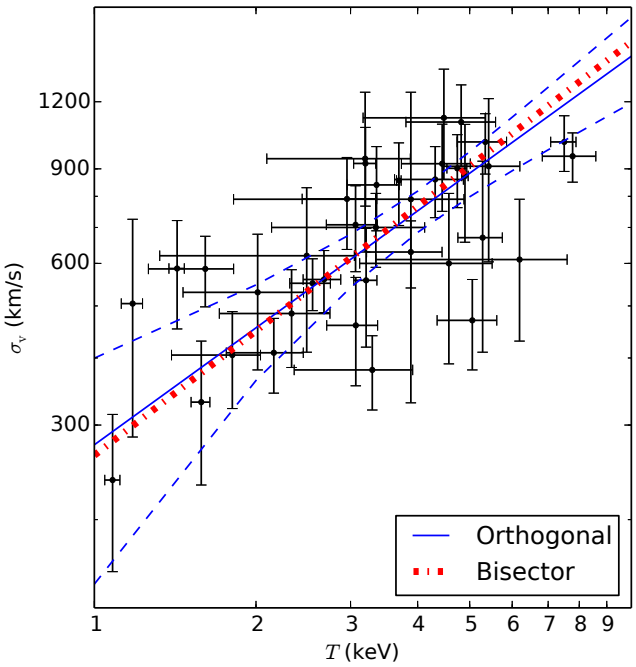

Figure 4. The σ_v–T relation assuming no evolution, i.e. $C = 0$ in Equation 3, for the combined sample. All lines are as explained in Fig. 3.

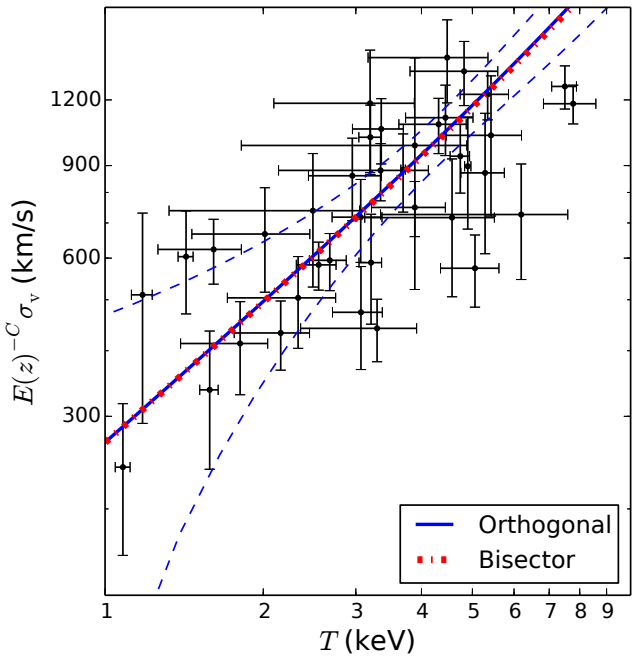

Figure 5. Plots showing the σ_v–T relation for the combined sample with varying evolution, i.e. C is a free parameter in Equation 3. The velocity dispersion is scaled to take into the account the evolution by multiplying by $E(z)^{-C}$. All lines are as explained in Fig. 3.

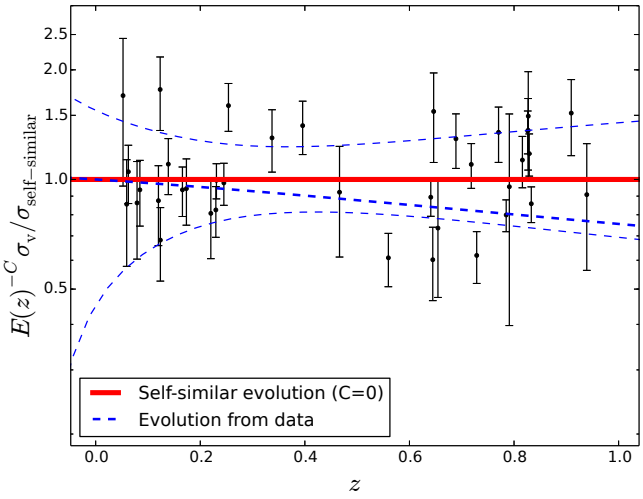

Figure 6. Plot showing the evolution of the normalisation of the $\sigma_v - T$ relation obtained for the data with the 95% confidence intervals in the dashed lines as compared to the self similar relation which predicts no evolution shown as the solid line. The black points show our sample data.

will be introduced, but it has been widely used for scaling relation measurements in the past and is therefore included for completeness.

Results from previous studies of the σ_v–T relation are collected in Table 1. All of these studies, except for Edge & Stewart (1991) and the low redshift sample of Wu et al. (1998), obtained a slope steeper than the expected self-similar slope of $\sigma_v \propto T^{0.5}$. We measured $B = 0.72 \pm 0.12$ using the orthogonal fitting method and $B = 0.77 \pm 0.08$ using the bisector fitting method for our combined sample. Therefore both the orthogonal and bisector slopes are in agreement with each other and the previous values in the literature, except for the result obtained by Edge & Stewart (1991) which is only consistent with the orthogonal result.

Except for work done by Wu et al. (1998) and Nastasi et al. (2014), all the previous results were obtained for low redshift samples and no test for evolution was performed. Wu et al. (1998) divided their sample into two groups, $z < 0.1$ and $z \geqslant 0.1$, and found no significant evolution, however their sample included only four clusters in the redshift range $0.5 < z < 1.0$. Nastasi et al. (2014) had a sample of 12 galaxy clusters and found a very large error of more than 50 per cent on their slope. They concluded that their sample size was too small to accurately measure evolution. We conclude that the data presented in this paper – a homogeneous cluster sample that is larger than those used in previous studies at $z > 0.5$ – are consistent with previous results.

5.2 Comparison with simulations - no evolution

Comparison to simulations are important for two main reasons. Firstly, we can determine if there is any bias due to sample selection as the simulations provide both a bigger temperature and redshift range. It also allows us to compare different simulation models and learn about the nature of the non-gravitational physics through their effect on the gas temperature.

The Millennium Gas Project is a set of hydrodynamical simulations described in Short et al. (2010) which uses the same initial perturbations as the Millennium Simulation (Springel et al. 2005). These simulations include a variety of models, including gravity

Table 6. Best fit values for the parameters in Equation 4 (slope, intercept and scatter) for the various models obtained from simulations without evolution. For the Millennium Gas Project we use dark matter (DM) and stars as the tracers for the velocity dispersion. The BAHAMAS simulation uses galaxies. The Millennium Gas simulations use spectroscopic like temperatures (T_{sl}) and the BAHAMAS simulation use spectroscopic temperatures (T_s).

Simulation	$\sigma_{\rm tracer}$	T_{model}	A	B	S
Millennium Gas	DM	T_{sl}	-0.011 $\pm$ 0.002	0.553 $\pm$ 0.008	0.028 $\pm$ 0.001
Millennium Gas	Stars	T_{sl}	-0.034 $\pm$ 0.003	0.621 $\pm$ 0.010	0.034 $\pm$ 0.001
BAHAMAS	Galaxies	T_s	-0.055 $\pm$ 0.003	0.848 $\pm$ 0.012	0.055 $\pm$ 0.001
BAHAMAS (Uniform T)	Galaxies	T_s	-0.122 $\pm$ 0.003	0.549 $\pm$ 0.015	0.025 $\pm$ 0.002

only; energy injection with radiative cooling; and feedback only. For comparison to the data presented in this paper, the feedback only model (FO) in a volume of $250\,h^{-1}$ Mpc^3 was used. This model includes supernova and AGN feedback using a semi-analytic galaxy formation model. Heating due to supernovae and AGN and the star formation rate are obtained using the model of De Lucia & Blaizot (2007). The AGN feedback model used is described in Bower et al. (2008), which is dependent on the matter accreted by the central black hole and the efficiency with which the matter is converted to energy near the event horizon, with the upper limit being at two per cent of the Eddington rate.

As a comparison to the velocity dispersion of the cluster, two proxies were considered, the velocity dispersion of the stars ($\sigma_{\rm Stars}$) and that obtained from the dark matter particles (σ_{DM}). The temperatures used from the simulation were spectroscopic-like temperatures ($T_{\rm sl}$; Mazzotta et al. 2004). To ensure that only clusters similar to those in our sample were included we excluded all groups from the simulation with a mass less than 10^{14} M$_\odot$. We also included a temperature cut, $1 < T\,({\rm keV}) < 11$, and a redshift cut, $0 < z < 1$, to match our sample.

We also compared to the results of the BAHAMAS hydrodynamical simulation (McCarthy et al., in prep. and Caldwell et al., in prep.). Here, a $400\,h^{-1}$ Mpc^3 box is used, with initial conditions based on Planck 2013 cosmological parameters (Planck Collaboration et al. 2014), and both AGN and supernovae feedback models as described by Le Brun et al. (2014). A galaxy mass lower limit of 5×10^9 M$_\odot$ and a cluster mass lower limit of 10^{14} M$_\odot$ were implemented. This simulation reproduces a large number of X-ray, SZ, and optical scaling relations of groups and clusters. However, unlike previous simulations, the new simulation also reproduces the observed galaxy stellar mass function remarkably well over a wide range of stellar masses. The velocity dispersion is traced by galaxies and is calculated using the gapper technique described by Beers et al. (1990). The temperatures used from the simulation were spectroscopic ($T_{\rm S}$).

For both sets of simulations the orthogonal fitting method described in Section 3.2 was applied with $C = 0$. The parameters A, B and S for both the Millennium Gas Project and BAHAMAS simulations are shown in Table 6. The $\sigma_{\rm v}$–T relation for the Millennium Gas Project with the two different $\sigma_{\rm v}$ proxies are shown in Fig. 7. The slope is slightly steeper for the stars (B=0.62 $\pm$ 0.01) than for the dark matter (B=0.55 $\pm$ 0.08) but both are consistent with previous studies of the $\sigma_{\rm v} - T$ relation and the results obtained from our data.

Fig. 8 shows that the orthogonal fit to the full BAHAMAS sample systematically overestimates the average velocity dispersion at $T > 5$ keV. This may be due, in part, to the model not being a complete description of the data: as can be seen in Fig. 8, the intrinsic scatter decreases with increasing temperature for the BAHAMAS sample. This is not captured in our orthogonal regression model (Equation 4), i.e. S is constant with both T and z. However, we found that this bias is mostly due to the temperature distribution of the sample. Choosing a subset of the BAHAMAS sample with a uniform temperature distribution, ie. a sample with the same number of clusters in each 0.01 keV bin, we obtained $B = 0.55 \pm 0.01$ using the orthogonal fitting method. We note that there is no single method which gives the underlying 'true' scaling relation in the presence of errors on both variables and intrinsic scatter: the recovered slope and normalisation depend upon the details of the method used.

5.3 The effect of biased slope measurements on the evolution of the normalisation

Having seen, using the BAHAMAS simulation, that the temperature distribution of the sample can affect the slope recovered using the orthogonal regression method, we now discuss the potential impact of a biased slope measurement on our conclusions regarding the observed cluster sample in Section 5.1. To investigate this, we generated 1000 mock samples (each containing 38 clusters) from the BAHAMAS simulation with the same temperature distribution as the observed sample, and applied the orthogonal regression method. Fig. 9 shows the distribution of recoverd slope values. The average is $B = 0.69 \pm 0.13$, which is 2σ higher than the slope obtained from the uniform T distribution sub-sample of BAHAMAS (Section 5.2). Therefore, *if* the BAHAMAS sample is representative of the real cluster population, then we would conclude that the slope we have measured for the observed cluster sample is biased high.

To check if such a biased slope estimate affects our conclusions regarding the lack of significant evidence for evolution of the normalisation of the relation (Section 4.2), we fixed the slope to $B = 0.5$ and re-ran the orthogonal fit for the observed cluster sample. We found $C = 0.15 \pm 0.28$, which is consistent with no evolution (Fig. 10). Therefore, even if the slope value of $B = 0.86 \pm 0.14$ that we measured was biased high for any reason, this does not affect our conclusion that we do not see significant evidence in favour of evolution.

5.4 Comparison with simulations - evolution

We now investigate evolution in the normalisation of the $\sigma_{\rm v}$–T relation in the simulations by fitting for the value of C, as we did for the observed sample (see Section 4.2). The results are shown in Table 7 and graphically in Fig. 11. The BAHAMAS simulation with free or fixed slope ($B = 0.5$) is consistent with zero evolution. However, the simulations from the Millennium Gas Project show small but significant positive evolution ($C = 0.273 \pm 0.013$ for σ_{Stars} and $T_{\rm sl}$). To see the reason for this, we can re-write the $\sigma_{\rm v}$–T relation in terms of the $\sigma_{\rm v}$–M and T–M relations, where M is the cluster mass (see, e.g., Maughan 2014). We define

$$\sigma_{\rm v} = 10^{A_{\sigma_{\rm v}T}} \left(\frac{T}{5\,{\rm keV}}\right)^{B_{\sigma_{\rm v}T}} E(z)^{C_{\sigma_{\rm v}T}}, \quad (9)$$

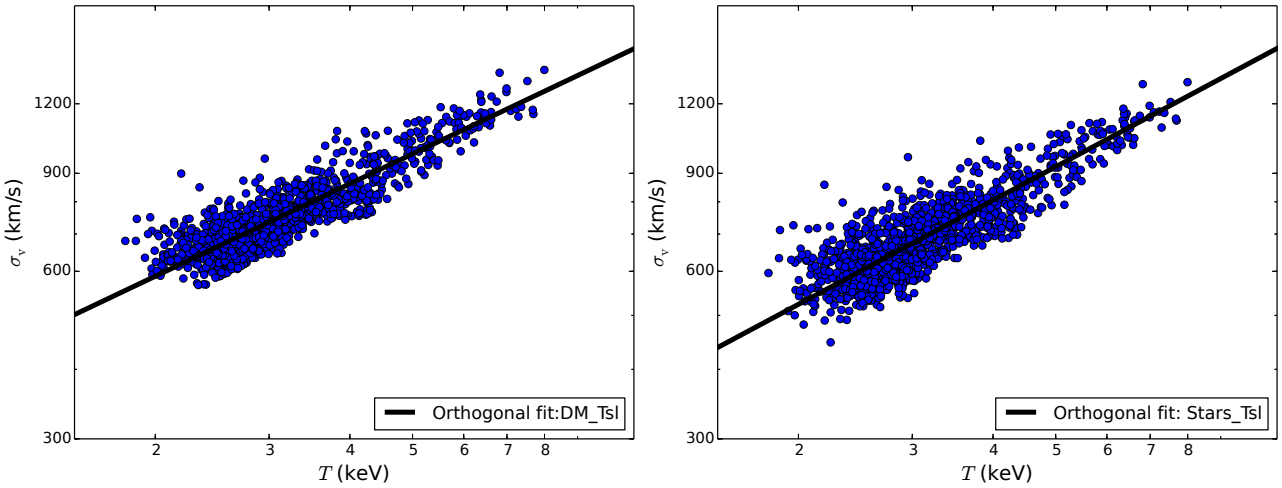

Figure 7. The σ_v–T relation for the Millennium Gas Project simulations using dark matter and stars as proxies for the velocity dispersion. The blue dots are the data obtained from the simulation and the solid black line shows the fit using the orthogonal regression method. The slope is slightly steeper for the stars (B=0.62 $\pm$ 0.01) than for the dark matter (B=0.55 $\pm$ 0.08) but both are consistent with previous studies of the $\sigma_v - T$ relation and the results obtained from our data.

Table 7. Best fit values for the parameters in Equation 4 (slope, intercept, scatter and evolution) for the various models obtained from simulations. All abbreviations are as in Table 6.

Simulation	$\sigma_{\rm tracer}$	T_{model}	A	B	S	C
Millennium Gas	DM	T_{sl}	-0.031 $\pm$ 0.002	0.551 $\pm$ 0.006	0.0220 $\pm$ 0.0010	0.371 $\pm$ 0.014
Millennium Gas	Stars	T_{sl}	-0.056 $\pm$ 0.002	0.619 $\pm$ 0.009	0.0295 $\pm$ 0.0010	0.397 $\pm$ 0.019
BAHAMAS (fixed B)	Galaxies	T_s	-0.135 $\pm$ 0.002	0.545	0.0390 $\pm$ 0.0010	0.046 $\pm$ 0.016
BAHAMAS (varying B)	Galaxies	T_s	-0.071 $\pm$ 0.005	0.779 $\pm$ 0.014	0.0570 $\pm$ 0.0010	-0.029 $\pm$ 0.024

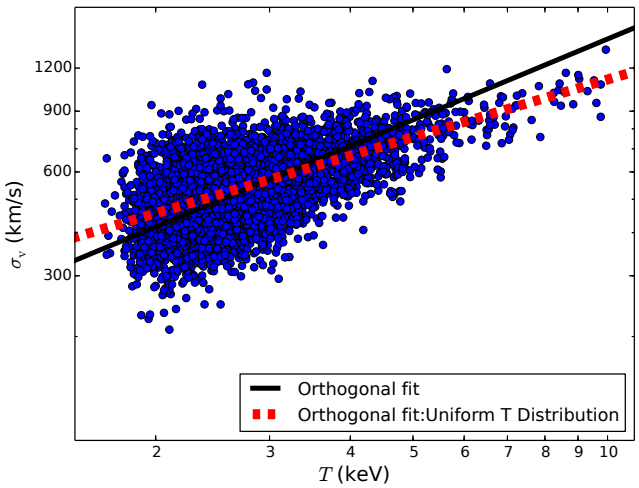

Figure 8. Plot showing the σ_v–T relation for the BAHAMAS simulation data. The blue circles represent the data points from the simulation. The solid line is the fit obtained using the orthogonal method. From this it can be seen that the orthogonal fit over-estimates the velocity dispersion at T_X >5 keV (see Section 6). A second fit was done to subset of the BAHAMAS simulation with a uniform T distribution, ie. the same number of clusters in each 0.01 keV bin, and this is shown by the dashed line.

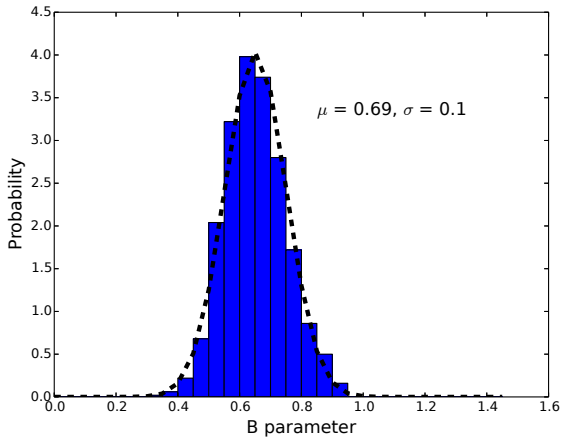

Figure 9. This histogram shows the probability of getting a specific value for the slope of the best-fit $\sigma_v - T$ relation given a mock cluster sample, drawn from BAHAMAS with temperature distribution matched to the observed cluster sample. We chose various subsamples from the BAHAMAS simulation which had the same T distribution as our sample and calculated the slope for each. The mean slope obtained is B=0.69$\pm$ 0.13, which is within 2 sigma of the value obtained from the uniform T sample shown in Figure 8, so there is a slight bias from the distribution of the sample.

where

$$B_{\sigma_v T} = B_{\sigma_v M}/B_{TM}\,,$$
$$A_{\sigma_v T} = A_{\sigma_v M} - A_{TM}B_{\sigma_v T}\,, \text{ and} \quad (10)$$
$$C_{\sigma_v T} = C_{\sigma_v M} - C_{TM}B_{\sigma_v T}\,.$$

Here, A, B and C have the same meaning as before, and the subscripts indicate the corresponding relation (e.g., B_{TM} indicates the slope of the T–M relation). If we set $C_{\sigma_v M} = 1/3$, $C_{TM} = 2/3$ and

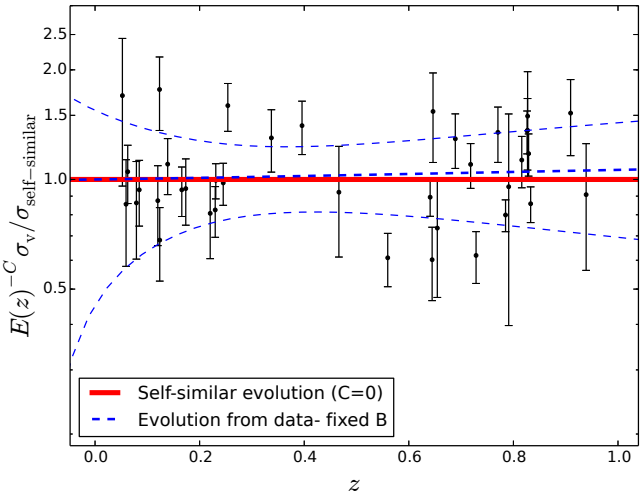

Figure 10. Plot showing the evolution of the normalisation of the $\sigma_v - T$ relation, with $B = 0.5$, obtained for the observed cluster sample with the 95% confidence intervals in the dashed lines, as compared to the self similar relation which predicts no evolution shown as the solid line. The black points show the measurements for the clusters in our sample.

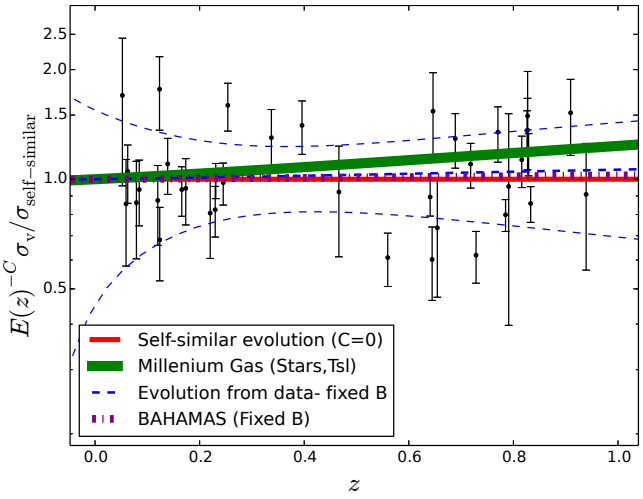

Figure 11. We compared the evolution of the normalisation of $\sigma_v - T$ relation of the Millennium Gas and BAHAMAS simulations with the self similar relation and that found from our data using a fixed slope. The solid line shows the line representing the self-similar relation i.e. $C = 0$, the dot-dashed line represents the BAHAMAS simulation results with a fixed B to avoid bias due to the sample distribution and the vertically dashed line represents the result from the Millennium Gas simulation. The blue dashed line and black points are our orthogonal fit and observed sample respectively.

$B_{\sigma_v T} = 1/2$ as predicted by the self-similar relation, then we obtain $C_{\sigma_v T} = 0$ as expected.

We performed fits to determine the values of $C_{\sigma_v M}$, C_{TM} and $B_{\sigma_v T}$ in the Millennium Gas simulation at $z = 0$ and $z = 0.5$. We found that $C_{\sigma_v M} = 1/3$ when using either σ_{Stars} or σ_{DM} as the measure of σ_v, and that $B_{\sigma_v T}$ varied from 0.55–0.6 (depending on whether spectroscopic-like or mass-weighted temperature estimates were used), which is slightly higher than the self-similar value, but not by enough to explain the positive evolution measured in the σ_v–T relation. This leads to the conclusion that the evolution is driven by the value of C_{TM}, and it was found that the measured value for the dark matter was $C_{TM} = 2/3$ as expected, but that this decreased to values between 0–0.2 for the gas. Therefore in the Millennium Gas simulation, the lack of redshift evolution in the $T - M$ relation drives the positive evolution in the σ_v–T relation.

The most likely explanation for the lack of redshift evolution in the $T - M$ relation in the Millennium Gas simulation is the absence of radiative cooling. When both cooling and feedback are included in simulations (as in BAHAMAS), the feedback acts as a regulation mechanism, heating the surrounding dense gas and expelling it from the cluster core. This in turn leads to higher-entropy gas flowing inwards. In the Millennium Gas simulation, the feedback model heats the gas and directly increases its entropy, which is eventually distributed throughout the cluster. This builds up over time as more and more energy is pumped into the gas from the growing black holes, and has the effect of slowing down the evolution of the $T - M$ relation (compared to the evolution expected due to the decreasing background density with redshift). This in turn leads to the positive evolution of the σ_v–T relation. It is likely that the more sophisticated feedback model used in BAHAMAS, where the entropy evolution is driven by radiative cooling, is the more realistic of the two.

6 CONCLUSIONS

We have studied the evolution of the velocity dispersion–temperature ($\sigma_v - T$) relation using a cluster sample spanning the range $0.0 < z < 1.0$ drawn from XCS. This work improves upon previous studies in terms of the use of a homogeneous cluster sample and the number of $z > 0.5$ clusters included. We present new redshift and velocity dispersion measurements based on Gemini data for 12 such $z > 0.5$ XCS clusters.

We used an orthogonal regression method to measure the normalisation, slope and intrinsic scatter of the σ_v–T relation for two subsamples: 19 clusters at $z < 0.5$, and 19 clusters with $z > 0.5$. In both cases, we found the slope of the relation to be consistent with the findings of previous studies, i.e., slightly steeper than expected from self-similarity.

Under the assumption that the slope of the relation does not evolve with redshift, we measured the evolution of the normalisation of the relation using the complete sample of 38 clusters. We found this to be slightly negative but not significantly different from the self-similar solution ($\sigma_v \propto T^{0.86\pm0.14} E(z)^{-0.37\pm0.33}$). Moreover, a no evolution model is the preferred choice when considering the Akaike Information Criterion.

We applied the same scaling relation analysis methods to the BAHAMAS and Millennium Gas cosmological hydrodynamical simulations. The σ_v–T relation does not evolve in BAHAMAS, in agreement with our findings for the observed cluster sample. However, positive evolution is seen in the Millennium Gas simulation. The difference is most likely due to the inclusion of self-consistent modelling of radiative cooling in BAHAMAS, which is absent in the Millennium Gas simulation. This leads to a very slowly evolving T–M relation in the Millennium Gas simulation, which in turn drives the positive evolution of the σ_v–T relation.

While this work has improved upon previous studies in terms of the number of high redshift clusters included, we note that the uncertainties on the scaling relation parameters are still rather large, and a combination of better measurements of individual cluster properties and a larger sample are required to make further progress.

ACKNOWLEDGEMENTS

SW and MH acknowledge financial support from the National Research Foundation and SKA South Africa. This research has made use of the NASA/IPAC Extragalactic Database (NED) which is operated by the Jet Propulsion Laboratory, California Institute of Technology, under contract with the National Aeronautics and Space Administration. Based on observations obtained at the Gemini Observatory, which is operated by the Association of Universities for Research in Astronomy, Inc., under a cooperative agreement with the NSF on behalf of the Gemini partnership: the National Science Foundation (United States), the National Research Council (Canada), CONICYT (Chile), the Australian Research Council (Australia), Ministério da Ciência, Tecnologia e Inovação (Brazil) and Ministerio de Ciencia, Tecnología e Innovación Productiva (Argentina). PAT acknowledges support from the Science and Technology Facilities Council (grant number ST/L000652/1). JPS gratefully acknowledges support from a Hintze Research Fellowship. STK acknowledges support from STFC (grant number ST/L000768/1).

REFERENCES

Beers T. C., Flynn K., Gebhardt K., 1990, AJ, 100, 32
Bird C. M., Mushotzky R. F., Metzler C. A., 1995, ApJ, 453, 40
Bower R. G., McCarthy I. G., Benson A. J., 2008, MNRAS, 390, 1399
Branchesi M., Gioia I. M., Fanti C., Fanti R., 2007, A&A, 472, 739
Burnham K. P., Anderson D. R., 2002, Model Selection and Multimodel Inference:A Practical Information-Theoretic Approach, 2 edn. Springer-Verlag, New York
Cash W., 1979, ApJ, 228, 939
Clerc N., Sadibekova T., Pierre M., Pacaud F., Le Fèvre J.-P., Adami C., Altieri B., Valtchanov I., 2012, MNRAS, 423, 3561
Clerc N., et al., 2014, MNRAS, 444, 2723
Cohn J. D., White M., 2005, Astroparticle Physics, 24, 316
Collins C. A., et al., 2009, Nature, 458, 603
Crawford S. M., Wirth G. D., Bershady M. A., 2014, ApJ, 786, 30
De Lucia G., Blaizot J., 2007, MNRAS, 375, 2
De Propris R., Couch W. J., Colless M., et al., 2002, MNRAS, 329, 87
Dickey J. M., 1990, in Thronson Jr. H. A., Shull J. M., eds, Astrophysics and Space Science Library Vol. 161, The Interstellar Medium in Galaxies. pp 473–481
Donahue M., Voit G. M., Scharf C. A., Gioia I. M., Mullis C. R., Hughes J. P., Stocke J. T., 1999, ApJ, 527, 525
Edge A. C., Stewart G. C., 1991, MNRAS, 252, 428
Ettori S., Tozzi P., Borgani S., Rosati P., 2004, A&A, 417, 13
Fadda D., Girardi M., Giuricin G., Mardirossian F., Mezzetti M., 1996, ApJ, 473, 670
Fassbender R., et al., 2011, New Journal of Physics, 13, 125014
Finn R. A., et al., 2005, ApJ, 630, 206
Gioia I. M., Wolter A., Mullis C. R., Henry J. P., Böhringer H., Briel U. G., 2004, A&A, 428, 867
Girardi M., Fadda D., Giuricin G., Mardirossian F., Mezzetti M., Biviano A., 1996, ApJ, 457, 61
Glazebrook K., Bland-Hawthorn J., 2001, PASP, 113, 197
Hasselfield M., et al., 2013, J. Cosmology Astropart. Phys., 7, 8
Hilton M., et al., 2009, ApJ, 697, 436
Hilton M., et al., 2010, ApJ, 718, 133
Hilton M., et al., 2012, MNRAS, 424, 2086
Hoekstra H., Herbonnet R., Muzzin A., Babul A., Mahdavi A., Viola M., Cacciato M., 2015, MNRAS, 449, 685
Hogg D. W., Bovy J., Lang D., 2010, preprint, (arXiv:1008.4686)
Kaiser N., 1986, MNRAS, 222, 323
Kay S. T., da Silva A. C., Aghanim N., Blanchard A., Liddle A. R., Puget J.-L., Sadat R., Thomas P. A., 2007, MNRAS, 377, 317
Kurtz M. J., Mink D. J., 1998, PASP, 110, 934
Le Brun A. M. C., McCarthy I. G., Schaye J., Ponman T. J., 2014, MNRAS, 441, 1270
Lloyd-Davies E. J., et al., 2011, MNRAS, 418, 14
Lubin L. M., Bahcall N. A., 1993, ApJ, 415, L17
Lumb D. H., et al., 2004, A&A, 420, 853
Magnelli B., Elbaz D., Chary R. R., Dickinson M., Le Borgne D., Frayer D. T., Willmer C. N. A., 2009, A&A, 496, 57
Mann A. W., Ebeling H., 2012, MNRAS, 420, 2120
Maughan B. J., 2014, MNRAS, 437, 1171
Maughan B. J., Jones L. R., Ebeling H., Scharf C., 2006, MNRAS, 365, 509
Maughan B. J., Giles P. A., Randall S. W., Jones C., Forman W. R., 2012, MNRAS, 421, 1583
Mazzotta P., Rasia E., Moscardini L., Tormen G., 2004, MNRAS, 354, 10
Mehrtens N., et al., 2012, MNRAS, 423, 1024
Mewe R., Schrijver C. J., 1986, A&A, 169, 178
Nastasi A., et al., 2014, A&A, 564, A17
Ortiz-Gil A., Guzzo L., Schuecker P., Böhringer H., Collins C. A., 2004, MNRAS, 348, 325
Planck Collaboration et al., 2014, A&A, 571, A16
Planck Collaboration et al., 2015, preprint, (arXiv:1502.01597)
Ponman T. J., Bourner P. D. J., Ebeling H., Böhringer H., 1996, MNRAS, 283, 690
Poole G. B., Babul A., McCarthy I. G., Fardal M. A., Bildfell C. J., Quinn T., Mahdavi A., 2007, MNRAS, 380, 437
Quintana H., Melnick J., 1982, AJ, 87, 972
Randall S. W., Sarazin C. L., Ricker P. M., 2002, ApJ, 577, 579
Reichardt C. L., et al., 2013, ApJ, 763, 127
Ritchie B. W., Thomas P. A., 2002, MNRAS, 329, 675
Rozo E., et al., 2009, ApJ, 699, 768
Sahlén M., et al., 2009, MNRAS, 397, 577
Schafer R. A., 1991, XSPEC, an x-ray spectral fitting package : version 2 of the user's guide
Short C. J., Thomas P. A., Young O. E., Pearce F. R., Jenkins A., Muanwong O., 2010, MNRAS, 408, 2213
Sifón C., et al., 2013, ApJ, 772, 25
Silverman J. D., et al., 2005, ApJ, 618, 123
Springel V., et al., 2005, Nature, 435, 629
Stott J. P., et al., 2010, ApJ, 718, 23
Tonry J., Davis M., 1979, AJ, 84, 1511
Tran K.-V. H., Kelson D. D., van Dokkum P., Franx M., Illingworth G. D., Magee D., 1999, ApJ, 522, 39
Vikhlinin A., van Speybroeck L., Markevitch M., Forman W. R., Grego L., 2002, ApJ, 578, L107
Vikhlinin A., Kravtsov A., Forman W., Jones C., Markevitch M., Murray S. S., Van Speybroeck L., 2006, ApJ, 640, 691
Vikhlinin A., et al., 2009, ApJ, 692, 1060
Voit G. M., 2005, Reviews of Modern Physics, 77, 207
White D. A., Jones C., Forman W., 1997, MNRAS, 292, 419
Wu X.-P., Fang L.-Z., Xu W., 1998, A&A, 338, 813
Wu X.-P., Xue Y.-J., Fang L.-Z., 1999, ApJ, 524, 22
Xue Y.-J., Wu X.-P., 2000, ApJ, 538, 65
von der Linden A., et al., 2014, MNRAS, 439, 2

APPENDIX A: OBSERVATIONS LOG

Table A1. Spectroscopic observations log. For all observations the R400 grating and the OG515 filter was used.

Cluster Name	Mask	Slits	Airmass Range	Observation Date	Frames(s)	Seeing (″)
XMMXCS J005656.6-274031.9	GS2012B–Q–011–03	33	1.22	2012–10–19	1 x 1830	
"	"		1.48 – 1.76	2012–10–16	2 x 1830	
"	"		1.01 – 1.04	2012–10–15	3 x 1830	0.76 – 0.80
"	GS2012B–Q–011–04	35	1.05 – 1.35	2012–11–14	4 x 1830	
XMMXCS J015241.1-133855.9	GS2011B–Q–050–01	33	1.05 – 1.21	2011–12–02	6 x 1830	
"	GS2011B–Q–050–02	34	1.05 – 1.65	2011–12–03	6 x 1830	
XMMXCS J021734.7-051326.9	GS2012B–Q–011–06	34	1.14 – 1.48	2012–12–05	4 x 1830	
XMMXCS J025006.4-310400.8	GS2012B–Q–011–09	32	1.11 – 1.20	2012–11–24	2 x 1830	
"	"		1.01 – 1.19	2012–11–21	4 x 1830	
"	GS2010B–Q–046–06	35	1.06 – 1.12	2010–11–14	2 x 1830	0.50 – 0.60
"	"		1.06 – 1.44	2010–11–13	5 x 1830, 1 x 762	1
XMMXCS J030205.1-000003.6	GS2011B–Q–050–03	32	1.17	2011–12–01	1 x 1830	
"	"		1.18	2011–11–20	1 x 1098	
"	"		1.17 – 1.45	2011–11–18	4 x 1830	
"	GS2011B–Q–050–04	32	1.32	2011–12–31	1 x 1098	
"	"		1.23 – 1.74	2011–12–30	4 x 1830	0.85 – 1.40
"	GS2011B–Q–050–05	33	1.27 – 1.57	2012–01–17	2 x 1830	0.7
XMMXCS J095940.7+023113.4	GS2010B–Q–046–02	35	1.19 – 1.23	2011–01–09	3 x 1830	
"	"		1.19 – 1.25	2011–01–08	4 x 1830	
"	GS–2012A–Q–46–01	35	1.19 – 1.29	2012–03–18	4 x 1830	
"	"		1.19 – 1.23	2012–03–02	2 x 1830	
"	GS–2012A–Q–46–02	34	1.20 – 1.35	2012–03–27	3 x 1830	
"	"		1.23 – 1.46	2012–03–23	3 x 1830	0.8
"	GS–2012A–Q–46–03	34	1.21 – 1.54	2012–03–22	6 x 1830	0.65 – 0.70
XMMXCS J112349.3+052956.8	GS–2012A–Q–46–05	33	1.23 – 1.33	2012–04–22	5 x 1830	
"	"		1.47	2012–04–21	1 x 1830	
"	GS–2012A–Q–46–06	32	1.25 – 1.65	2012–05–15	4 x 1830	0.63 – 0.76
"	"		1.45 – 1.66	2012–04–22	2 x 1830	
"	GS2010B–Q–046–03	33	1.26	2011–01–31	1 x 1830	
"	"		1.35 – 1.64	2011–01–29	2 x 1525, 1 x 975	
"	"		1.23 – 1.24	2011–01–27	2 x 1830	
XMMXCS J113602.9–032943.2	GS–2012A–Q–46–07	36	1.14	2012–05–24	1 x 1830	
"	"		1.12	2012–05–23	1 x 1830	
"	"		1.12 – 1.16	2012–05–20	3 x 1830	
"	"		1.12	2012–05–19	1 x 1830	
"	GS–2012A–Q–46–08	33	1.48 – 1.76	2012–07–15	2 x 1830	
"	"		1.41 – 1.80	2012–07–11	3 x 1830	0.50 – 0.70
"	"		1.5	2012–07–10	1 x 1830	
XMMXCS J134305.1-000056.8	GS–2012A–Q–46–10	36	1.16 – 1.23	2012–05–24	4 x 1830	
"	"		1.24	2012–05–21	1 x 1830	
"	GS–2012A–Q–46–11	34	1.25	2012–07–10	1 x 1830	
"	"		1.16 – 1.19	2012–07–09	2 x 1830	
"	"		1.2	2012–07–06	1 x 1830	
"	"		1.54 – 1.84	2012–06–22	2 x 1830	
XMMXCS J145009.3+090428.8	GN2012A–Q–070–05	32	1.02 – 1.05	2012–07–09	2 x 1800	1.15
"	"		1.11 – 1.62	2012–06–26	4 x 1800	0.84 – 0.98
"	GN2012A–Q–070–06	34	1.02 – 1.04	2012–07–07	2 x 1800	
"	"		1.09 – 1.17	2012–07–06	2 x 1800	
"	"		1.48 – 1.79	2012–06–27	2 x 1800	
"	GN2012A–Q–070–07	33	1.22 – 1.59	2012–07–22	3 x 1800	
"	"		1.04 – 1.16	2012–07–08	3 x 1800	1
XMMXCS J215221.0–273022.6	GS2010B–Q–046–04	36	1.14 – 1.24	2010–11–12	2 x 1830	
"	"		1.02 – 1.21	2010–09–14	4 x 1830	
"	GS2011B–Q–050–06	34	1.07 – 1.15	2011–10–05	2 x 1830	
"	"		1.12 – 1.56	2011–09–18	4 x 1830	0.60 – 1.00
"	GS2011B–Q–050–07	34	1.00 – 1.10	2011–10–24	4 x 1830	
"	"		1.05 – 1.12	2011–10–16	2 x 1830	
XMMXCS J230247.7+084355.9	GN2012A–Q–070–10	34	1.37	2012–08–08	1 x 1800	0.60 – 0.68
"	"		1.02 – 1.11	2012–07–30	5 x 1800	0.43 – 0.86
"	GN2012A–Q–070–11	33	1.18 – 1.31	2012–08–13	2 x 1800	
"	"		1.02 – 1.08	2012–08–09	3 x 1800	0.60 – 0.68
"	"		1.19	2012–08–08	1 x 1800	1

APPENDIX B: REDSHIFT CATALOGUE

Tables of galaxy redshifts measured in each cluster to appear in the online version of the article.